Available online at www.sciencedirect.com
ScienceDirect
Trans. Nonferrous Met. Soc. China 35(2025) 2288−2303
Transactions of Nonferrous Metals Society of China
www.tnmsc.cn

Twinning mechanism and grain size model of hot deformed FGH4113A alloy

Jun-cheng ZHU[1,2], Yong-cheng LIN[1,2,3], Zi-jian CHEN[1,2], Yong-fu XIE[4], Jin YANG[4], Majid NASERI[5]

1. School of Mechanical and Electrical Engineering, Central South University, Changsha 410083, China;
2. State Key Laboratory of Precision Manufacturing for Extreme Service Performance, Central South University, Changsha 410083, China;
3. Rongcheng Huadong Metal-forming Machinery Co. Ltd., Rongcheng 264300, China;
4. Guizhou Anda Aviation Forging Co. Ltd., Anshun 561005, China;
5. South Ural State University, 76 Lenin Av., Chelyabinsk 454080, Russia

Received 28 June 2024; accepted 17 January 2025

Abstract: The effects of varying strain rates and deformation temperatures on the microstructure evolution of the FGH4113A alloy were investigated through hot compression experiments. During hot deformation, grain evolution is primarily governed by dynamic recrystallization (DRX) and twinning primarily. Furthermore, the pinning effect of the primary γ' phase (γ'_p phase) plays a crucial role in grain refinement. Lower strain rates or higher temperatures facilitate DRX, twinning, and the dissolution of the γ'_p phase. At 1140 °C, significant dissolution of the γ'_p phase and the subsequent loss of its pinning effect reduce twinning activity. A unique twinning mechanism, termed "pinning twinning", is identified, occurring exclusively under the influence of the pinning effect. When grain boundary migration fails to accommodate dislocations due to the pinning effect, grains preferentially eliminate dislocations via twinning, thereby reducing local strain energy. The grain size prediction model is improved by considering the pinning effect.
Key words: nickel-based superalloy; hot deformation; dynamic recrystallization; twinning; γ' phase; pinning effect

1 Introduction

The nickel-based powder metallurgy (P/M) superalloys possess exceptional mechanical properties, fatigue resistance, and corrosion resistance, which makes them ideal materials for manufacturing advanced aerospace engine turbine disks [1,2]. The superior performance of nickel-based P/M superalloys relies on their fine and uniform grain structure, as well as the dispersed distribution of strengthening particles [3−5]. The primary precipitate particle in these alloys is the γ' phase [6−8]. The presence of a coarse primary γ' phase (referred to as γ'_p phase) exerts a pinning effect on grain boundaries, thereby hindering their migration and inhibiting grain growth [9,10]. Techniques such as isothermal forging, which involve large plastic deformations, are commonly employed to shape nickel-based P/M superalloys [11−13]. Therefore, investigating the evolution of grain structure and the influence of γ'_p phase on this process during hot deformation of nickel-based P/M superalloys is essential. This research is pivotal for controlling the microstructure and properties of superalloy by post-isothermal forging.

In recent years, some researchers have investigated the evolution of grain structure of nickel-based superalloys during hot deformation [14−16]. YANG et al [17] found that the changes in grain structure and size in nickel-based P/M superalloys during the hot deformation are mainly

Corresponding author: Yong-cheng LIN, E-mail: yclin@csu.edu.cn
https://doi.org/10.1016/S1003-6326(25)66815-4

influenced by dynamic recrystallization (DRX). They developed a model to predict DRX grain size, showing that higher deformation temperature and lower strain rate lead to larger DRX grains. CHEN et al [18] emphasized twinning as a key deformation mechanism in fine-grained nickel-based P/M superalloys, which is attributed to the high volume fraction of γ' phase that hinders slip. LI et al [19] observed that twinning predominantly occurs during DRX grain growth in nickel-based P/M superalloys subjected to hot deformation, with increasing temperatures facilitating twinning to reduce free energy. However, an increased temperature leads to the consumption of free energy through grain boundary migration, reducing the twin content. Additionally, WEN et al [20] indicated that the dispersed γ'_p phases in nickel-based P/M superalloys hinder grain boundary migration, thereby aiding grain refinement. ZHU et al [21] demonstrated that increasing temperature and decreasing strain rate lead to the dissolution of γ'_p phases, which in turn reduces the hindrance to grain boundary migration in nickel-based P/M superalloys. SONG and AINDOW [22] suggested that the limiting grain size reflects the strength of the γ' phase pinning effect, which is directly proportional to the size of γ' phase and inversely proportional to its volume fraction. A smaller limiting grain size corresponds to a stronger pinning effect. Collectively, these studies provide a theoretical foundation for examining grain structure evolution, twinning, and the pinning effect of γ'_p phases in nickel-based P/M superalloys during hot deformation.

There are some reports on twinning in nickel-based superalloys [23−25]. However, existing researches reveal inconsistency in the trend of twin content variation in nickel-based superalloys, primarily due to variations in microstructures [19,26,27]. Previous studies have explored the pinning effect in superalloys [28−30], revealing significant variations in both the strength and impact of this effect across different microstructures. The FGH4113A alloy, which is the focus of this study, is characterized by a high volume fraction of uniformly distributed γ'_p phases, distinguishing it from other nickel-based superalloys. This unique microstructure results in a more pronounced pinning effect in the FGH4113A alloy compared to other alloys, where variations in γ'_p phase content significantly affect microstructure evolution. Consequently, understanding the pinning effect and its impact on twinning during hot deformation is essential.

This study aimed to optimize the isothermal forging processing window of the hot-extruded (HEXed) FGH4113A alloy by investigating the evolution and interaction mechanisms of microstructures during hot compression deformation. The influence of DRX and twinning on grain evolution was analyzed. Furthermore, the pinning effect of the primary γ' phase (γ'_p phase) on grain refinement was discussed. The effective range of the pinning effect was defined, leading to the development of a grain size prediction model that would offer theoretical guidance for industrial manufacturing practices.

2 Experimental

A novel P/M superalloy, FGH4113A, consists of the following chemical composition (wt.%): 12.8−13.3 Cr, 18.5−19.5 Co, 3.5−3.9 Ti, 2.8−3.2 Al, 0.17−0.23 Hf, 0.9−1.1 Ta, 1.1−1.3 Nb, 3.8−4.3 Mo, 3.8−4.3 W and Bal. Ni. The FGH4113A alloy billets were produced via vacuum induction melting (VIM), followed by argon atomization and hot isostatic pressing (HIP) at 1150 °C and 150 MPa for 4 h. Subsequently, the billets were extruded using a hot extrusion (HEX) at 1110 °C with a ratio of 4.7∶1 and a speed of 35 mm/s.

Figure 1(a) illustrates the grain structure of HEXed FGH4113A alloy obtained by electron backscatter diffraction (EBSD, JEOL−7001F1 FE-SEM), which has an average grain size of 3.32 μm. Figures 1(b, c) present the γ' phases in the HEXed FGH4113A alloy as observed using scanning electron microscope (SEM, TESCAN MIRA3 LMU). The micrographs reveal the presence of two distinct phases: the γ'_p phase and the secondary γ'phase (γ'_sphase), with the γ matrix located in the interstices between the γ' phases. The volume fraction and average size of γ'_p phases are 43.69% and 2.72 μm, respectively, which are comparable to grain dimensions. This configuration suggests that the grain structure remains fine after the HEX process due to the significant pinning effect of abundant coarse γ'_p phases, effectively suppressing grain growth at high temperatures.

Additionally, the thermally induced pole (TIP)

is one of the primary defects that develop during the HIP of P/M superalloys. Also, porosity has a substantial impact on the mechanical properties of the alloy. In this study, the HIP process effectively reduces porosities in the HEXed FGH4113A alloy. Given the well-established nature of HIP technology for nickel-based superalloys, few thermally induced pores were observed [31]. Moreover, HEX can further enhance the density of the alloy structure.

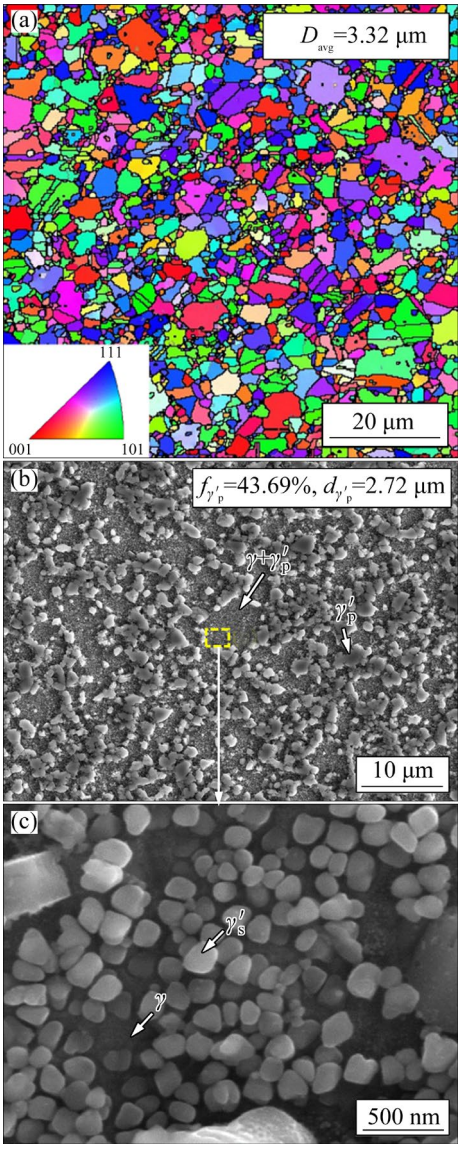

Fig. 1 Initial microstructures of HEXed FGH4113A alloy: (a) EBSD map; (b, c) SEM micrographs

Hot compression tests were performed on the HEXed FGH4113A alloy using a Gleeble−3500D thermomechanical simulator, with true strains of 0.22, 0.51, and 0.92 applied. The primary objective of these tests was to analyze the grain evolution and the interaction mechanisms between γ'_p phases and grains during hot deformation. Cylindrical samples measuring d8 mm × 12 mm were extracted from a HEXed FGH4113A billet. The hot compression tests utilized deformation temperatures of 1050, 1080, 1110, and 1140 °C, along with strain rates of 1, 0.1, 0.01, and 0.001 s^{-1}. Tantalum foil was applied to both sides of specimens, along with the lubricant, to minimize the effects of friction on the material flow behavior. After preheating all specimens to the target deformation temperature at a rate of 10 °C/s, 300 s holding time was utilized to ensure uniform temperature distribution prior to loading. Following hot compression tests, specimens were rapidly quenched in chilled water to preserve the deformed microstructure, as depicted in Fig. 2, which outlines the experimental steps.

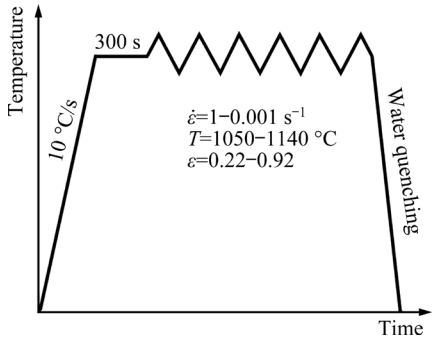

Fig. 2 Hot compression experimental process and deformation conditions

Deformed samples underwent axial cutting for microstructural analysis. Initially, the specimens were mechanically polished using diamond plaster to create a reflective surface suitable for SEM observation. Subsequently, electrolytic polishing was carried out using a solution of 30% H_2O and 70% H_3PO_4 at room temperature for 10−30 s. The specimen thickness was reduced to 60−100 μm through mechanical grinding to facilitate the examinations by EBSD, transmission electron microscopy (TEM, Titan G2 60-300), and X-ray energy dispersive spectrometer (EDS) examination. Standard discs with a diameter of 3 mm were punched out from the specimens, followed by a double spray electrolysis process using a solution of 10 mL $HClO_4$ and 90 mL CH_3CH_2OH. Electrolysis was conducted within a temperature range from −30 to −20 °C at a constant voltage of 20 V. EBSD analysis utilized a scan area of 80 μm × 80 μm with

a step size of 0.2 μm and a accelerating voltage of 25 kV. In this study, data related to grain structure were processed using HKL Channel 5 software. Data concerning γ'_p phases were obtained through Image Pro Plus software. Velox software and Gatan Digital Micrograph 3.9 were employed for processing TEM and EDS observations.

3 Results and discussion

3.1 Effects of deformation parameters on grain structure

3.1.1 Impact of strain rate

Figures 3(a−c) show the distribution of grain-orientation spread (GOS) in the HEXed FGH4113A alloy following hot deformation at 1110 °C with various strain rates, reaching a maximum strain of 0.92. Thick black lines represent grain boundaries, thin black lines denote subgrain boundaries, and red lines signify Σ3 twin boundaries. Previous studies have shown that the twin boundaries in nickel-based superalloys primarily consist of Σ3 twin boundaries [19,32]. This study aims to investigate the twinning behavior of the HEXed FGH4113A alloy through analyzing Σ3 twin boundaries. The GOS distribution figures quantify the average deviation of individual pixel orientations within a grain from the average grain orientation, thereby offering insights into residual dislocation density within each grain. Grains exhibiting a GOS greater than 3 are classified as deformed grains [17]. The microstructure reveals that a small number of deformed grains coexist with a predominant quantity of DRX grains [33,34]. Certain DRX grains exhibit relatively high dislocation densities (2<GOS<3), formed early in the deformation process, and subsequently, dislocations (Fig. 3(d)) present grain distribution data acquired through HKL Channel 5 software. X_{drx} represents the DRX volume fraction and D_{avg} denotes the average grain size. Furthermore, during grain growth, grain boundaries attempt to move away from the γ'_p phases, necessitating the formation of new boundaries at the original sites of γ'_p phases. To reduce the increase in grain boundary area and interfacial energy, the γ'_p phases located at the grain boundaries exert forces that inhibit both migration and grain growth. This phenomenon is known as the pinning effect of the γ'_p phases on the grain boundaries [35,36]. D_{lim} signifies the limiting

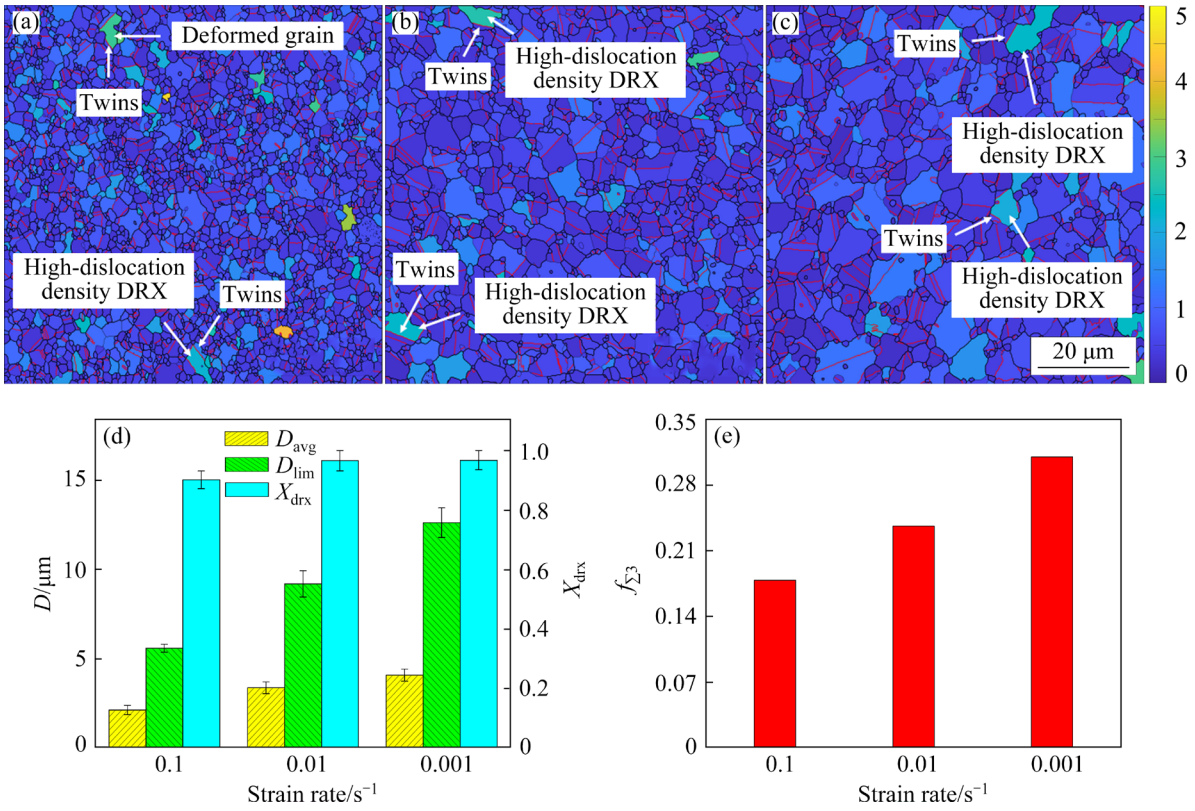

Fig. 3 GOS maps of HEXed FGH4113A alloy deformed at T=1110 °C, ε=0.92 and different strain rates of 0.1 s^{-1} (a), 0.01 s^{-1} (b) and 0.001 s^{-1} (c); Grain size and volume fraction of DRX (d); Σ3 boundary fraction (e)

grain size, representing the maximum size a single grain can achieve due to the pinning effect. It excludes the influence of dynamic recrystallization (DRX) grains that have not yet been formed or interacted with the γ'_p phases, thereby illustrating the strength of pinning effect [22,29,30].

As the strain rate decreases, the DRX volume fraction gradually increases and reaches saturation. This is attributed to lower strain rates, which extend deformation time, allowing the alloy to absorb more heat energy and promoting DRX growth. DRX growth gradually envelops the deformed grains, leading to an increase in D_{ave}. Moreover, D_{lim} increases with decreasing strain rate, corresponding to enhanced energy absorption and grain growth. However, if γ'_p phases at low strain rates exert the same pinning effect as observed at high strain rates, it would not be feasible to increase the grain growth limit. It is suggested that the pinning effect weakens with decreasing strain rate. The driving force for grain growth arises from the reduction in local strain energy, prompting grain boundaries to migrate from regions of dislocation density to others [37,38]. Consequently, the observed increases in D_{avg} and D_{lim} are attributed to the growth of DRX grains, while the size of deformed grains decreases. Figure 4 presents SEM micrographs and data statistics of the same alloy deformed under the conditions in Fig. 3, revealing a significant distribution of γ'_p phases along grain boundaries (GBs). $f_{\gamma'_p}$ and $d_{\gamma'_p}$ represent the volume fraction and average size of γ'_p phases, respectively. As the strain rate decreases, $f_{\gamma'_p}$ gradually decreases. Lower strain rates result in increased heat energy and longer dissolution time, which facilitate element diffusion and enhance the dissolution of γ'_p phases. Conversely, $d_{\gamma'_p}$ increases gradually with decreasing strain rate, although it remains lower than that observed in the HEXed condition. Higher strain rates promote the refinement of γ'_p phases through splitting. At elevated strain rates, dislocations lack sufficient time to be consumed. Instead, they accumulate around the γ'_p phase, causing stress concentration, which contributes to the splitting and refinement of the γ'_p phase [39,40]. Conversely, lower strain rates lead to a smaller $f_{\gamma'_p}$ and a larger $d_{\gamma'_p}$, indicating that fewer γ'_p phases per unit volume produce a pinning effect, which implies a weaker pinning effect consistent with earlier analyses regarding D_{lim}.

Significant twinning phenomena are observed in Figs. 3(a−c). Figure 3(e) depicts the proportion of Σ3 twin boundaries relative to the total grain

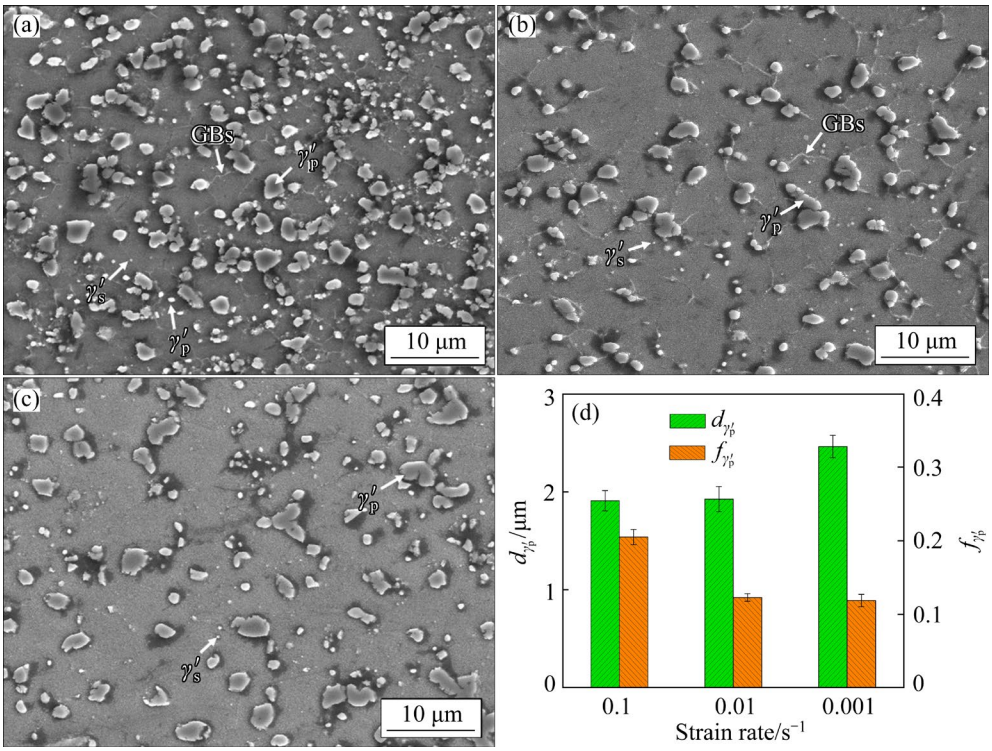

Fig. 4 SEM micrographs of HEXed FGH4113A alloy deformed at T=1110 °C, ε=0.92 and different strain rates of 0.1 s^{-1} (a), 0.01 s^{-1} (b) and 0.001 s^{-1} (c); Average grain size and volume fraction of γ'_p phase (d)

boundaries at different strain rates, showing an increase in this proportion as the strain rate decreases. A decrease in strain rate reduces the pinning effect of the γ'_p phase on the DRX grain boundaries, providing sufficient time and additional energy for their migration. Additionally, twinning primarily occurs as a byproduct of DRX grain boundary migration during hot deformation [19,41]. Stacking fault in atomic layers may inadvertently occur during grain boundary migration. If the atomic layers stack in an opposite order along the stacking fault, the stacking fault evolves into a twin. An increased frequency of grain boundary migration correlates with a greater likelihood of atomic layer stacking faults. Consequently, lower strain rates promote DRX growth and grain boundary migration, thereby increasing the likelihood of twinning. Furthermore, twinning occurs in some deformed grains or DRX grains characterized by high dislocation density, with significant notable variations in dislocation density observed on each side of the twin boundary. This indicates that such twinning occurs within grains with a high accumulation of dislocations, leading to a significant drop in dislocation density in post-twinning. The reduction in dislocation density, which lowers local strain energy, initiates this type of twinning. Therefore, during hot deformation of the HEXed FGH4113A alloy, apart from DRX growth incidents, a twinning mechanism operates to minimize local strain energy.

3.1.2 Impact of deformation temperature

Figure 5 illustrates the GOS maps and statistical data on the grain distribution of the HEXed FGH4113A alloy, subjected to hot deformation at a strain rate of 0.01 s^{-1} and various temperatures, reaching a strain of 0.92. As the deformation temperature increases, both X_{drx} and D_{avg} increase gradually. Higher temperature contributes additional heat energy to the alloy, promoting DRX nucleation and the migration of DRX grain boundaries. This phenomenon envelops deformed grains, leading to an increase in X_{drx} and subsequently an increase in D_{avg}. Figure 6 shows SEM micrographs and relevant data under same deformation conditions as those in Fig. 5 (SEM micrograph at 1110 °C and 0.01 s^{-1} is depicted in Fig. 4(b)). With increasing the deformation temperature, the $f_{\gamma'_p}$ decreases gradually. This decrease is attributed to the higher temperature providing increased heat energy, which enhances the atomic diffusion rates and results in a greater

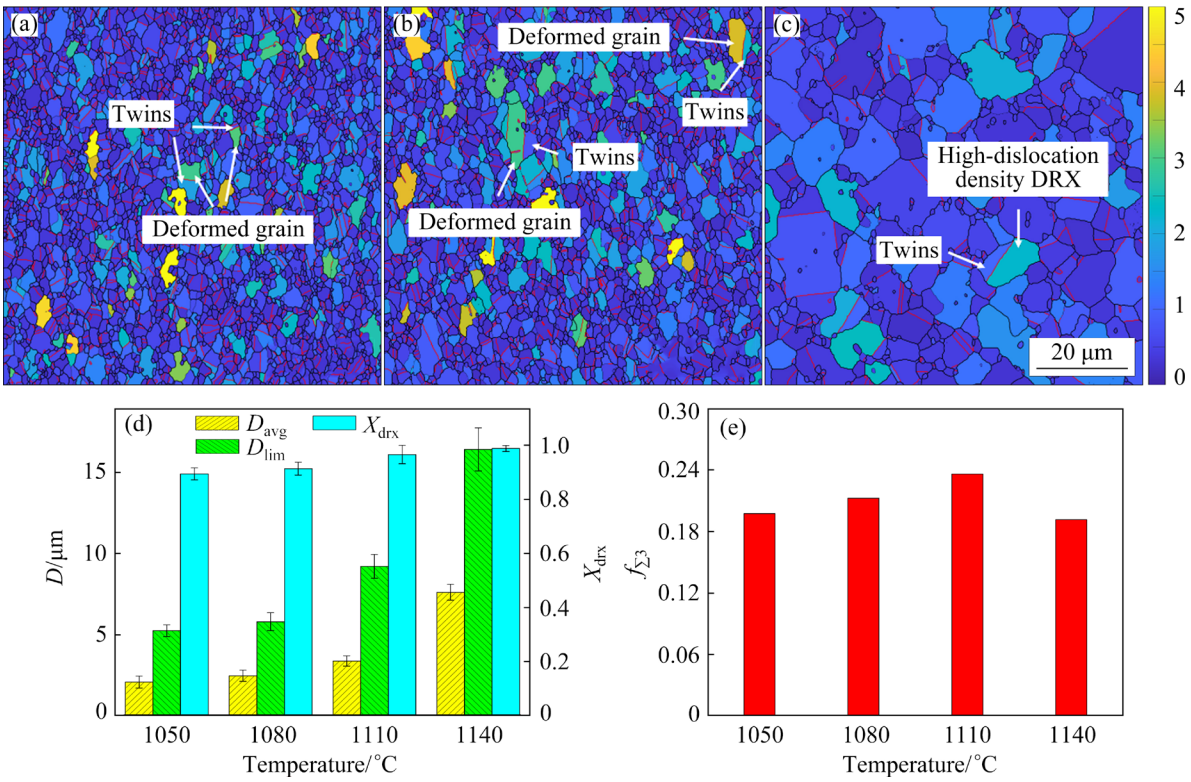

Fig. 5 GOS maps of HEXed FGH4113A alloy deformed at $\dot{\varepsilon}$ =0.01 s^{-1}, ε=0.92 and different temperatures of 1050 °C (a), 1080 °C (b), and 1140 °C (c); Drain size and volume fraction of DRX (d); Σ3 boundary fraction (e)

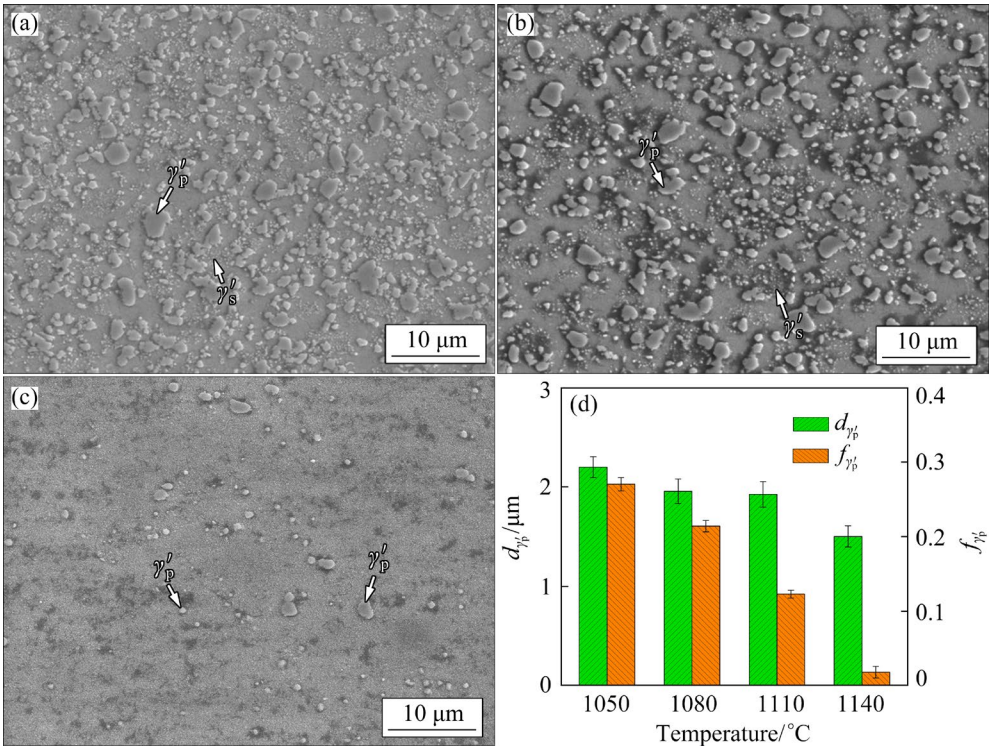

Fig. 6 SEM micrographs of HEXed FGH4113A alloy deformed at $\dot{\varepsilon}$=0.01 s^{-1}, ε=0.92 and different temperatures of 1050 °C (a), 1080 °C (b), and 1140 °C (c); Average grain size and volume fraction of γ'_p phase (d)

dissolution of γ'_p phases during the same deformation period. Consequently, the value of $d_{\gamma'_p}$ decreases gradually with increasing temperature. Although both $f_{\gamma'_p}$ and $d_{\gamma'_p}$ decrease simultaneously, an increase in D_{lim} with temperature remains evident in Fig. 5(d). This indicates that as temperature rises, the pinning effect of γ'_p phase on grains continues to weaken. Thus, $f_{\gamma'_p}$ plays a critical role in determining the strength of the pinning effect during the hot deformation of the HEXed FGH4113A alloy. Furthermore, while the values of D_{avg} and D_{lim} increase consistently with temperature, their rate of increase at 1050−1110 °C remains relatively steady before rising significantly at 1140 °C. Thus, it is suggested that although the pinning effect of the γ'_p phase diminishes as temperature increases, it remains significant within the temperature range of 1050−1110 °C. At 1140 °C, although the γ'_p phase presents in the alloy and hinders the migration of certain grain boundaries, its overall pinning effect becomes ineffective at a macroscopic level.

Figure 5(e) illustrates how the Σ3 twin boundary proportion changes in relation to total grain boundary count at various deformation temperatures. The proportion of Σ3 twin boundaries increases initially, followed by a decline with increasing deformation temperature. At the temperatures between 1050 and 1110 °C, elevated temperatures promote DRX and lead to a higher occurrence of twinning. However, at 1140 °C, a notable decrease in the proportion of Σ3 twin boundaries occurs. This reduction is attributed to the inhibition of grain growth and dislocation consumption caused by the pinning effect of the γ'_p phase in the lower temperature range of 1050−1110 °C. Under these conditions, grains necessitate twinning to alleviate local strain energy. Conversely, at 1140 °C, the alloy's pinning effect diminishes, allowing for unrestricted grain growth. Dislocations can now be consumed by DRX grain boundary migration, negating the necessity for twinning to reduce local strain energy. As twinning is governed by the pinning effect, it is termed "pinning twinning". Consequently, the substantial reduction in pinning twinning at 1140 °C, relative to other temperatures, leads to a decrease in the proportion of Σ3 twin boundaries.

3.2 γ'_p phase characteristics

Figure 7 depicts the morphology and elemental composition of the γ'_p phases. Figure 7(a) illustrates

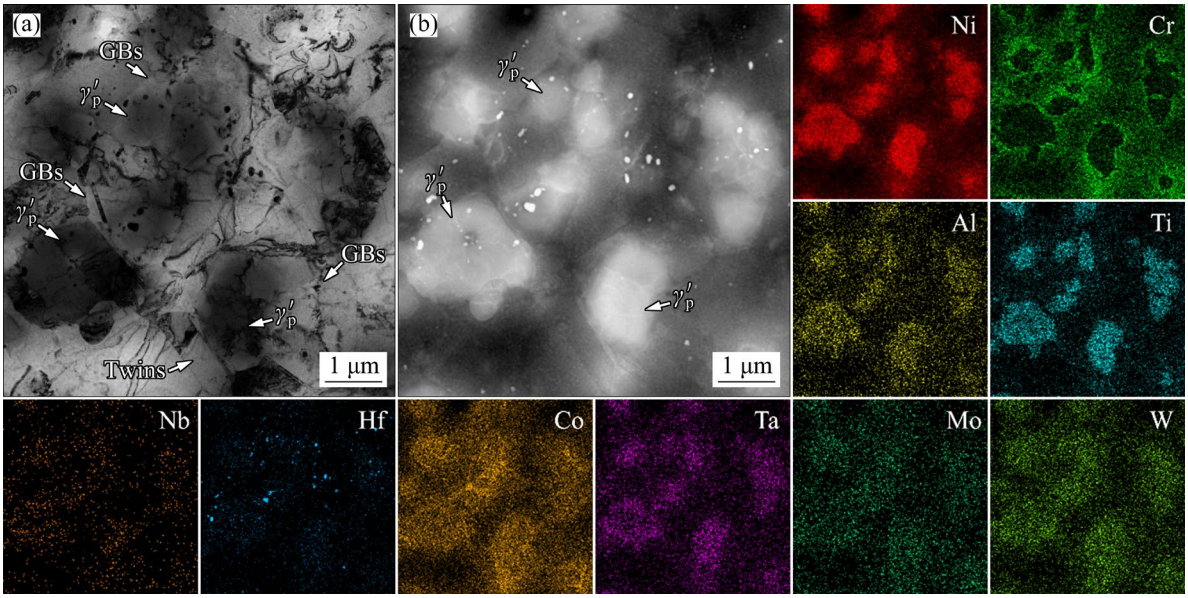

Fig. 7 TEM mapping of γ'_p phase: (a) TEM morphology; (b) TEM-HAADF image

the TEM morphology of the γ'_p phases, highlighting their predominant distribution along the grain boundaries. Figure 7(b) shows the TEM-HAADF (high-angle annular dark field) image, revealing that the γ'_p phases have higher contrast compared to γ grains. Ni, as the main constituent of the FGH4113A alloy, is distributed in both γ grains and γ'_p phases, showing significant enrichment in the latter. The principal constituents of the γ'_p phases are $Ni_3(Al,Ti)$, which are characterized by substantial enrichment of Al and Ti. Cr, the primary inhibitory element precipitating in the γ'_p phases, accumulates in the γ grains but is absent from the γ'_p phases [42,43]. Moreover, Co, Ta, Mo, and W are enriched compared to other elements, such as Cr, Nb and Hf, in the γ'_p phase. At elevated temperatures, Co preferentially substitutes Ni to form $(Ni,Co)_3(Al,Ti)$, while elements such as Ta, Mo, and W typically occupy the Al atomic sites [44]. Research indicates that the addition of Co, Ta, Mo, and W modifies the lattice parameter of the γ'_p phase, thereby enhancing its shear modulus [44]. An increase in shear modulus increases the energy required for the grain boundary to traverse the γ'_p phase, thereby strengthening the pinning effect within the alloy [45].

3.3 Pinning twinning mechanism

Figure 8 shows TEM images of the HEXed FGH4113A alloy, which was deformed at 1080 °C and 0.01 s^{-1}, reaching a strain of 0.92. In Fig. 8(a), numerous γ'_p phases are dispersed around grains, and there are plentiful dislocations and twinning within the grains. Figure 8(c) presents the TEM-HAADF image of the same region, providing a clearer view of γ'_p phases surrounding the grains. The γ'_p phases are aligned along grain boundaries in multiple orientations. Figure 8(b) depicts TEM morphology from a different orientation, compared to Fig. 8(a), which emphasizes the interactions between grain boundaries and dislocations. The dislocations are present within the grains, leading to high local strain energy. To alleviate local strain energy in grains, grain boundaries migrate along the yellow arrows and absorb dislocations in grains. Numerous bulges (indicated by red arrows) develop on the grain boundaries, indicating a propensity for migration. However, the presence of γ'_p phases at the grain boundaries generates a pinning effect, which hinders migration of grain boundaries towards regions of high dislocation density, thereby preventing dislocation consumption. This process preserves the overall straightness of the grain boundaries but introduces serrated features, clearly demonstrating the pinning effect [21,46,47]. Consequently, grains can only alleviate local strain energy through twinning.

Figure 8(d) displays the high-resolution transmission electron microscopy (HRTEM) image along with its fast Fourier transform (FFT) graph,

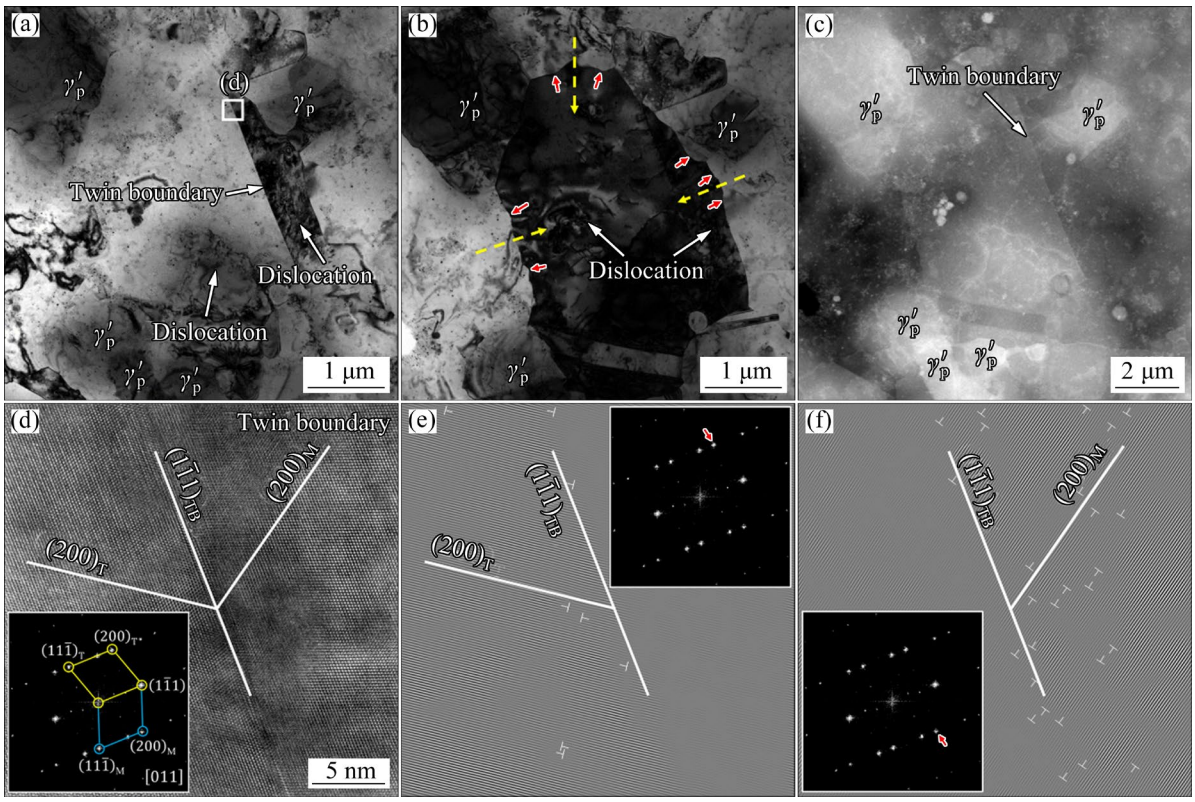

Fig. 8 TEM images of HEXed FGH4113A alloy deformed at 1080 °C and 0.01 s^{-1} (ε=0.92): (a, b) TEM morphology; (c) TEM- HAADF image; (d) HRTEM image of twin boundary; (e, f) Inverse FFT graphs of (200)

revealing a twin boundary in the area shown in Fig. 8(a), characterized by distinct twinning relationships. Figures 8(e, f) display the inverse FFT graphs of face-centered cubic (FCC) (200) lattice planes on both sides of twin boundary, highlighting a significant accumulation of incompletely consumed dislocations near the boundary. The left side of the twin boundary exhibits a considerably lower dislocation density compared to the right side, indicating that the grain on the left side reduces local strain energy by consuming dislocations through twinning. Twinning facilitates dislocation consumption via two mechanisms: first, by absorbing dislocations within the grain during the formation of twin boundaries; second, by altering the grain's orientation, which liberates the newly formed grain boundaries from the pinning effect, allowing for continued migration.

Pinning twinning primarily occurs when dislocations cannot be consumed through DRX grain growth, attributed to a pinning effect on grains. A previous study [31] demonstrated that, at high temperatures and low strain rates, DRX grain growth is the primary mechanism for dislocation consumption in the FGH4113A alloy. Conversely, at low temperatures and high strain rates, dislocations are predominantly eliminated through DRX nucleation. The presence of γ'_p phases neither inhibits nor hinders this process; rather, it actively facilitates it. As a result, the likelihood of pinning twinning occurring similarly to DRX grain growth events increases with increasing temperature and decreasing strain rate. However, when the temperature increases or strain rate decreases beyond a specific threshold, the extensive dissolution of γ'_p phases leads to the loss of their pinning effect, significantly reducing the likelihood of pinning twinning. This aligns with the findings in Sections 3.1.

3.4 Criterion of pinning effect

The aforementioned research demonstrates that the pinning effect can significantly limit grain growth and facilitate twinning, thereby profoundly affecting the microstructure of FGH4113A alloy. In Section 3.1.2, it is revealed that, at higher temperatures, even if the γ'_p phase remains partially

undissolved, the pinning effect does not impact the entire alloy significantly. Hence, determining the effective range of the pinning effect in the alloy is essential for controlling the microstructure of the FGH4113A alloy. Since $f_{\gamma'_p}$ is crucial for assessing the efficacy of the pinning effect and represents a broader characteristic compared to $d_{\gamma'_p}$, it provides a better depiction of overall state of γ'_p phase in the alloy, thereby enhancing manageability during hot forming. Accordingly, this study uses $f_{\gamma'_p}$ as the criterion for assessing the pinning effect in the alloy.

Previous research has shown that a critical grain size exists in alloy growth due to the pinning effect of second phase particles, which is related to the properties of the particles [22]. This study further explores and demonstrates this relationship:

$$D_{\lim} = \alpha \frac{d_{\gamma'_p}}{f_{\gamma'_p}^{n}} \tag{1}$$

where α and n are material constants.

Equation (1) can be expressed as

$$\frac{D_{\lim}}{d_{\gamma_p}} = \alpha f_{\gamma'_p}^{-n} \tag{2}$$

Equation (1) indicates that $D_{\lim}/d_{\gamma'_p}$ is inversely proportional to $f_{\gamma'_p}$ (where n is a positive number). Figure 9(a) illustrates the relationship between $D_{\lim}/d_{\gamma'_p}$ and $f_{\gamma'_p}$ under varying deformation conditions. It is evident that, at high values of $f_{\gamma'_p}$, $D_{\lim}/d_{\gamma'_p}$ shows a gradual rise as $f_{\gamma'_p}$ decreases, indicating the occurrence of pinning effect under these deformation conditions. In contrast, at low values of $f_{\gamma'_p}$, there is a notable increase in $D_{\lim}/d_{\gamma'_p}$ with decreasing $f_{\gamma'_p}$, suggesting that the γ'_p phase has lost its pinning effect. Figure 9(b) presents the data from Fig. 9(a) on a logarithmic scale, offering a clearer distinction in the relationship between $D_{\lim}/d_{\gamma'_p}$ and $f_{\gamma'_p}$ in the two datasets. When the pinning effect is present, the corresponding values of α and n are 1.08 and 0.736, respectively. Conversely, when the pinning effect diminishes, the values shift to 2.53 and 0.373, respectively. The intersection of the two curves occurs at the point of $f_{\gamma'_p}$=0.096, serving as the threshold to determine the presence of the pinning effect in the alloy.

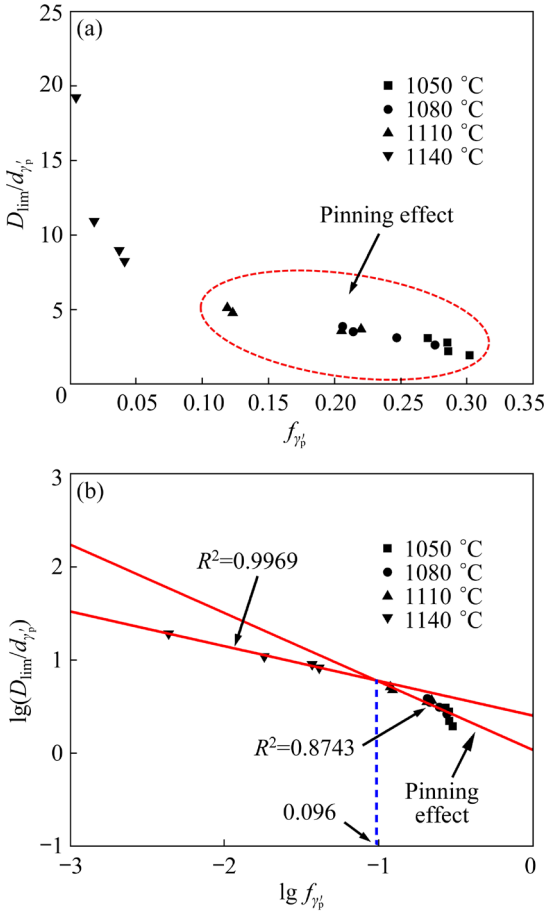

Fig. 9 Relationship between $D_{\lim}/d_{\gamma'_p}$ and $f_{\gamma'_p}$

3.5 DRX grain size model considering pinning effect

Table 1 summarizes the deformation conditions selected according to the criteria outlined in Section 3.4, which exhibit a pinning effect, along with the corresponding D_{drx} values stabilized at ε=0.92. These D_{drx} values, influenced by DRX grain growth during hot deformation, increase with increasing temperature and decreasing strain rate. DRX grain growth is a thermally activated process, with higher temperatures supplying the necessary driving force for this phenomenon. Elevated temperatures also accelerate the migration rate of grain boundaries, resulting in an increased rate of DRX grain growth. At high strain rates, the short duration of deformation inhibits the growth of DRX grains. Generally, the relationship among DRX grain size, deformation temperature, and strain rate can be expressed as [17]

$$D_{drx} = A_d \dot{\varepsilon}^{m_d} \exp\left(-\frac{Q_d}{RT}\right) \tag{3}$$

Table 1 D_{drx} values under pinning effect after deformation stabilization

T/°C	D_{drx}/μm			
	1 s^{-1}	0.1 s^{-1}	0.01 s^{-1}	0.001 s^{-1}
1050	0.92	1.11	2.01	2.56
1080	1.18	1.39	2.39	3.82
1110	2.04	2.12	3.37	4.08

where D_{drx} is DRX grain size, T is deformation temperature, R is molar gas constant, and A_d, m_d, and Q_d are material parameters. Taking the logarithm of Eq. (3) gives

$$\ln D_{drx} = \ln A_d + m_d \ln \dot{\varepsilon} - \frac{Q_d}{RT} \tag{4}$$

Figure 10 illustrates the relationship between $\ln D_{drx}$ and $\ln \dot{\varepsilon}$ under these deformation conditions, as well as between $\ln D_{drx}$ and $1/T$. The values of A_d, m_d and Q_d were determined using the nonlinear least squares method. Therefore, the DRX grain size model of the HEXed FGH4113A alloy during hot deformation under the pinning effect can be established as

$$D_{drx} = 1.09\times10^{6}\,\dot{\varepsilon}^{-0.149} \exp\left(-\frac{1.54\times10^{5}}{RT}\right) \quad \left(f_{\gamma'_p} \geq 0.096\right) \tag{5}$$

Figure 11 presents a comparison between the calculated and experimental DRX grain sizes. To evaluate the predictive capability of the model, the correlation coefficient (R) and average absolute relative error (AARE) are computed, i.e.,

$$R = \frac{\sum_{i=1}^{N}\left(E_i - \overline{E}\right)\left(P_i - \overline{P}\right)}{\sqrt{\sum_{i=1}^{N}\left(E_i - \overline{E}\right)^2\left(P_i - \overline{P}\right)^2}} \tag{6}$$

$$\text{AARE} = \frac{1}{N}\sum_{i=1}^{N}\left|\frac{E_i - P_i}{E_i}\right| \times 100\% \tag{7}$$

where E_i denotes the experimental value, while P_i denotes the corresponding calculated value. $\overline{E}$ and $\overline{P}$ indicate the mean values of E_i and P_i, respectively, while N stands for the total number of samples used for comparison. R merely indicates the linear relationship between E_i and P_i, whereas AARE provides a more direct measure of the model's accuracy. The R is 0.9671, accompanied by an AARE of 9.44%. The high R values and low errors indicate that this model can accurately predict the DRX grain size of the HEXed FGH4113A alloy during hot deformation influenced by the pinning effect.

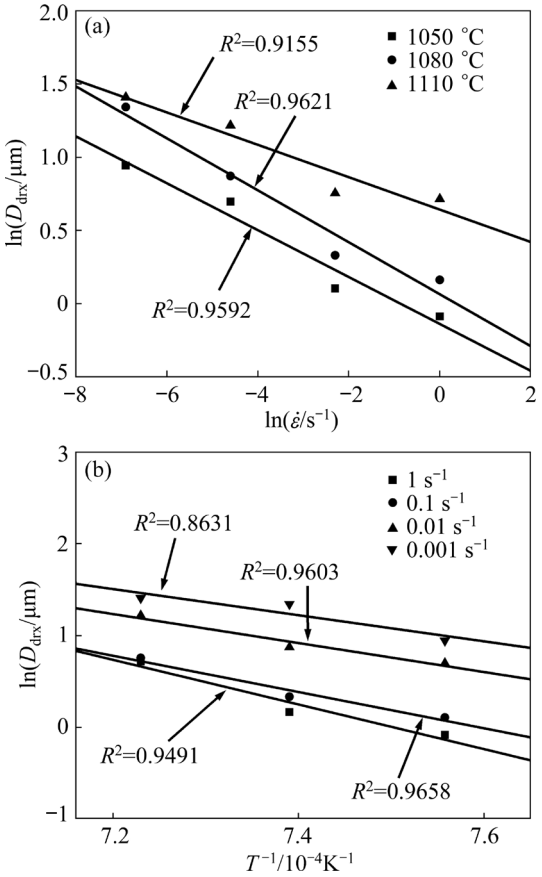

Fig. 10 Relationship of parameters in DRX grain size model of HEXed FGH4113A alloy: (a) $\ln D_{drx}$–$\ln \dot{\varepsilon}$; (b) $\ln D_{drx} - 1/T$

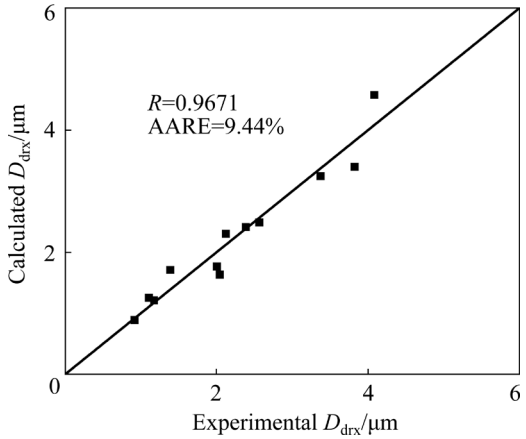

Fig. 11 Comparison between calculated and experimental D_{drx}

3.6 Average grain size model considering pinning effect

Commonly, it is believed that D_{avg} is related to D_{drx} and X_{drx} in the following formulation [48]:

$$D_{avg}=D_{drx}X_{drx}+D_0(1-X_{drx}) \quad (8)$$

where D_0 represents the size of deformed grains in the HEXed FGH4113A alloy, calculated based on the initial grain size. D_{avg} under the pinning effect is calculated using Eq. (8) under various deformation conditions. To validate the accuracy of predictive models, this study utilized the predicted values of D_{drx} from Eq. (5) for prediction purposes.

Subsequently, ten sets of calculated values that highlight key features were chosen from the data collected under various deformation conditions and compared with experimental values, as illustrated in Fig. 12. The corresponding deformation conditions for each set are listed in Table 2.

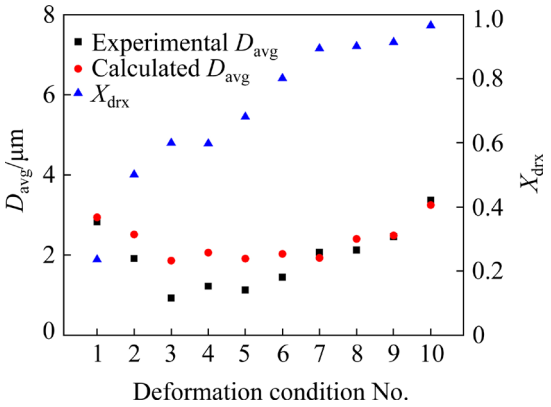

Fig. 12 Comparisons between calculated and experimental D_{avg} under different deformation conditions

Table 2 Corresponding deformation conditions

Number	Deformation temperature/°C	Strain rate/s^{-1}	Strain
1	1080	0.1	0.22
2	1080	0.1	0.51
3	1050	1	0.92
4	1080	1	0.92
5	1050	0.1	0.92
6	1080	0.1	0.92
7	1050	0.01	0.92
8	1110	0.1	0.92
9	1080	0.01	0.92
10	1110	0.01	0.92

Notably, a significant discrepancy between calculated and experimental values is observed under deformation conditions of Nos. 3−6, indicating inaccuracies in the predictions derived from Eq. (8). This discrepancy is attributed to the phenomenon where deformed grains are either engulfed or fractured by DRX due to nucleation and growth processes, leading to a decrease in deformed grain size (D_0). When the size of deformed grains is considerably larger than that of DRX grain (i.e., $D_0 \gg D_{drx}$), the decrease in D_0 can be neglected in the calculations involving Eq. (8). However, the fine grain structure and the pinning effect prevented excessive growth of both deformed grains and DRX grains during hot deformation. As a result, their sizes remained similar, which made the significant reduction in D_0. Therefore, directly utilizing Eq. (8) to calculate D_{avg} resulted in considerable errors. Under deformation condition of No.1, where X_{drx} is low, indicating a reduced extent of DRX, there was less engulfment and fewer breaks in deformed grains, resulting in smaller errors from the reduced D_0. In contrast, under deformation conditions of Nos. 7−10, higher X_{drx} values reduce the contribution of $D_0(1-X_{drx})$ in Eq. (8), thereby minimizing the impact of D_0 reduction on the calculated outcomes.

In this study, experimental data are utilized to determine the specific variables n_a and D_{drx}. n_a is not constant. It decreases as the extent of reduction in D_0 increases. In Fig. 12, X_{drx} values under deformation conditions of Nos. 3 and 4 are similar. However, based on Eq. (10), the calculated n_a are −0.0476 and 0.219, respectively. This discrepancy arises because the reduction in D_0 does not correlate linearly with the increase in X_{drx}. A increased number of DRX nucleation sites results in a more pronounced decrease in D_0.

In order to reduce the calculation error and reflect the reduction in D_0, an exponential factor, n_a, is proposed, i.e.,

$$D_{avg}=D_{drx}X_{drx}+D_0^{n_a}\left(1-X_{drx}\right) \quad (9)$$

$$n_a=\log_{D_0}\left(\frac{D_{avg}-D_{drx}X_{drx}}{1-X_{drx}}\right) \quad (10)$$

Figure 13 illustrates the engulfment/breakage processes of the deformed grains at various DRX nucleation levels. At low levels of DRX nucleation, DRX can only enclose deformed grains by growing

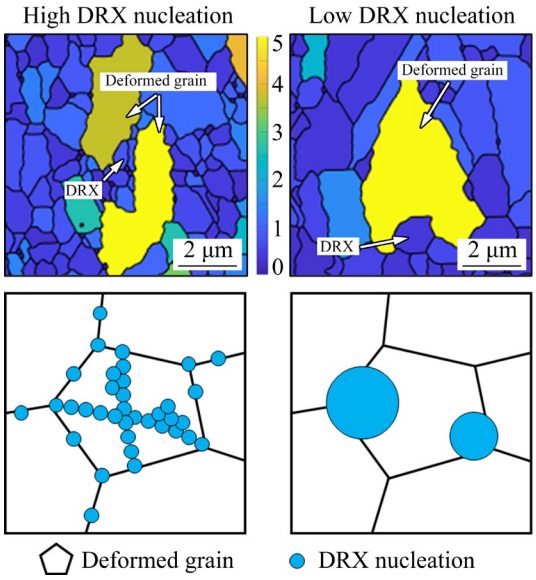

Fig. 13 Engulfment/breakage mechanisms of deformed grains at different DRX nucleation levels

around them, causing a minor reduction in D_0 and an increase in n_a. Conversely, higher levels of DRX nucleation enhance the likelihood of DRX formation at new DRX/deformed grain boundaries. As DRX pervades the entire deformed grain, it directly divides the grain, leading to a substantial decrease in D_0 and a reduction in n_a. Both X_{drx} and D_{drx} were analyzed using statistical methods on 2D images processed with HKL Channel 5 software. The density of DRX nucleation per unit area is directly proportional to X_{drx}/D_{drx}^2, implying that n_a is inversely related to X_{drx}/D_{drx}^2. Theoretically, DRX exclusively induces a decrease in D_0, and thus $n_a \leq 1$. Figure 14 illustrates the correlation between the experimental n_a and X_{drx}/D_{drx}^2, indicating that the curve can be well-fitted with a high R^2 value when it has an intercept of 1. The subsequent equation is derived through fitting:

$$n_a = -1.46\frac{X_{drx}}{D_{drx}^2} + 1.00 \tag{11}$$

Hence, the expression for D_{avg} can be expressed as

$$\begin{cases} D_{avg} = D_{drx}X_{drx} + D_0^{n_a}\left(1 - X_{drx}\right) \\ n_a = -1.46\dfrac{X_{drx}}{D_{drx}^2} + 1.00 \end{cases} \quad \left(f_{\gamma'_p} \geq 0.096\right) \tag{12}$$

Figure 15 presents a comparison between the calculated and experimental D_{avg}, showing R value of 0.9629 and AARE of 8.62%. The high R values and small error demonstrate that this model can accurately predict the average grain size of the HEXed FGH4113A alloy during hot deformation influenced by pinning effect.

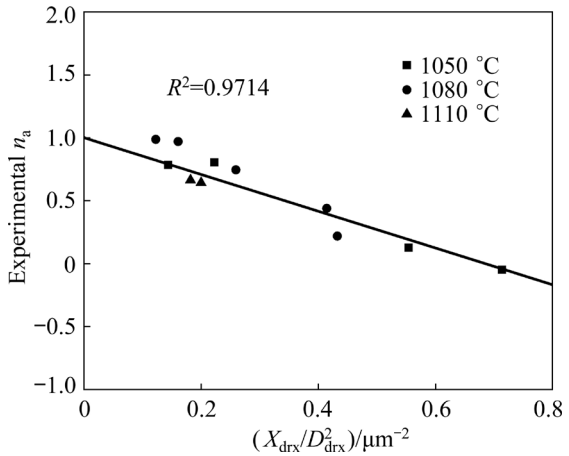

Fig. 14 Relationship between experimental n_a and X_{drx}/D_{drx}^2

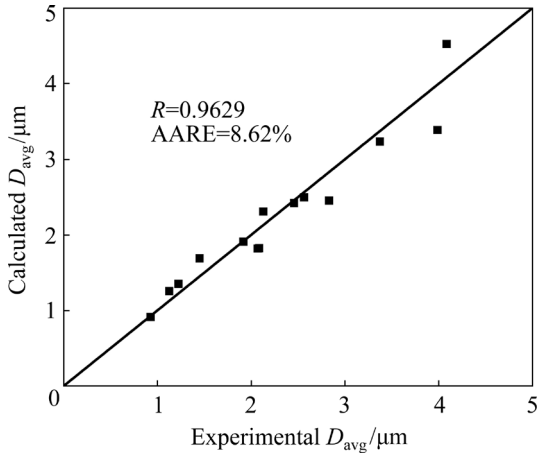

Fig. 15 Comparison between calculated and experimental D_{avg}

4 Conclusions

(1) The pinning effect of γ'_p phase significantly impacts the grain structure of the HEXed FGH4113A alloy. With increasing temperature and decreasing strain rate, the γ'_p phase dissolves, thereby weakening the pinning effect and promoting grain growth.

(2) A twinning mechanism termed “pinning twinning” is observed in deformed grains and DRX grains with high dislocation density influenced by the pinning effect. In scenarios where dislocations are predominantly consumed by DRX grain growth, the pinning effect hinders dislocation consumption through grain boundary migration. Consequently,

grains consume dislocations through twinning, breaking away from the pinning effect and restarting grain boundary migration. The reduction in local strain energy drives the occurrence of pinning twinning.

(3) At higher temperatures, the pinning effect becomes ineffective, leading to considerable grain growth and diminished pinning twinning. Analysis of D_{lim} under various deformation conditions suggests that a volume fraction of γ'_{p} phase below 0.096 renders the pinning effect within the alloy ineffective.

(4) Models have been developed to predict DRX grain size and average grain size considering the pinning effect. In the model for predicting D_{avg}, the parameter (n_{a}) is incorporated to quantify the reduction in deformed grain size, thereby improving the model's accuracy. Both models effectively forecast DRX grain size and average grain size under varying deformation conditions.

CRediT authorship contribution statement

Jun-cheng ZHU: Data curation, Investigation, Writing − Original draft; **Yong-cheng LIN:** Conceptualization, Methodology, Supervision, Writing − Review & editing; **Zi-jian CHEN:** Data curation, Investigation; **Yong-fu XIE:** Data curation, Investigation; **Jin YANG:** Data curation, Investigation; **Majid NASERI:** Data curation, Investigation.

Declaration of competing interest

The authors declare that they have no known competing financial interests or personal relationships that could have appeared to influence the work reported in this paper.

Acknowledgments

This work was supported by the National Key Research and Development Program of China (No. 2022YFB3706902), and Innovation Project for Graduate Students of Hunan Province, China (No. 1053320212786). This work was supported in part by the High Performance Computing Center of Central South University, China.

References

[1] REED R C. The superalloys: Fundamentals and applications [M]. Cambridge, England: Cambridge University Press, 2006.

[2] WU Yu-ting, LI Chong, XIA Xing-chuan, LIANG Hong-yan, QI Qi-qi, LIU Yong-chang. Precipitate coarsening and its effects on the hot deformation behavior of the recently developed γ'-strengthened superalloys [J]. Journal of Materials Science & Technology, 2021, 67: 95−104.

[3] JANEIRO I S, FRANCHET J M, CORMIER J, BOZZOLO N. Dynamic precipitation during forging of a γ–γ' nickel-based superalloy [J]. Metallurgical and Materials Transactions A, 2023, 54(5): 2052−2070.

[4] SCHULZ B, LEITNER T, HAFOK M, PRIMIG S. Advancements in processing of Ni-based superalloys by microstructure engineering via discontinuous γ' break-down [J]. Materialia, 2023, 31: 101873.

[5] IMAYEV V, MUKHTAROV S, MUKHTAROVA K, GANEEV A, SHAKHOV R, PARKHIMOVICH N, LOGUNOV A. Influence of forging and heat treatment on the microstructure and mechanical properties of a heavily alloyed ingot-metallurgy nickel-based superalloy [J]. Metals, 2020, 10(12): 1606.

[6] ZHANG Zhi-yang, DING Ran, GUO Qian-ying, LIU Chen-xi, LIU Yong-chang. Improving the microstructural stability and tensile properties of Inconel 617 superalloy at high temperature by stabilization of the γ' phase [J]. Journal of Materials Research and Technology, 2024, 29: 2991−2998.

[7] TAN Gang, LI Hui-zhong, WANG Yan, YANG Lei, QIAO Shi-chang, HUANG Zheng-qin, LIU Min-xue. Hot working characteristics of HEXed PM nickel-based superalloy during hot compression [J]. Transactions of Nonferrous Metals Society of China, 2020, 30(10): 2709−2723.

[8] ZHANG Yang, FAN Yue-ming, FENG Kai-li, LU Chao-ze, WANG Yi-han, SHAO Tian-min. Evolution of high-temperature hardness of multimodal γ' nickel-based superalloy [J]. Journal of Materials Research and Technology, 2024, 29: 3771−3781.

[9] YANG Qiu-mei, LIN Yong-cheng, LIU Guan, CHEN Zi-jian, QIU Yu-liang, WU Gui-cheng, ZHU Jun-cheng. Morphological evolution and dissolution mechanisms of γ' phase in a novel HIPed P/M superalloy in hot deformation process [J]. Journal of Alloys and Compounds, 2023, 947: 169653.

[10] JI Zhi-yong, JIA Chong-lin, PAN Xing-yu, QIU Chun-lei. Grain growth kinetics and γ' dissolution behavior of a novel disc superalloy GH4065A [J]. JOM, 2023, 75(12): 5884−5892.

[11] LIU Wei, LIU Zhi-ling, ZHANG Hua, RUAN Jing-jing, HUANG Hai-liang, ZHOU Xin, MENG Fan-chao, ZHANG Shang-zhou, JIANG Liang. Hot deformation behavior and new grain size model of hot extruded FGH4096 superalloy during hot compression [J]. Journal of Alloys and Compounds, 2023, 938: 168574.

[12] LI Hui-zhong, YANG Lei, WANG Yan, TAN Gang, QIAO Shi-chang, HUANG Zheng-qin, LIU Min-xue. Thermal deformation and dynamic recrystallization of a novel HEXed P/M nickel-based superalloy [J]. Materials Characterization, 2020, 163: 110285.

[13] BUCKINGHAM R C, ARGYRAKIS C, HARDY M C, BIROSCA S. The effect of strain distribution on microstructural developments during forging in a newly developed nickel base superalloy [J]. Materials Science and Engineering A, 2016, 654: 317−328.

[14] SCHULZ B, HAGHDADI N, LEITNER T, HAFOK M, PRIMIG S. Dynamic recrystallisation via nucleation at distorted twins in a Ni-based superalloy [J]. Journal of Alloys and Compounds, 2023, 936: 168318.

[15] ERIKSSON E, HANNING F, ANDERSSON J, COLLIANDER M H. Dynamic recrystallization during hot compression of Ni-based superalloy Haynes 282 [J]. Journal of Alloys and Compounds, 2023, 960: 170837.

[16] ZHANG Mu-xin, ZHANG Bei-jiang, JIAO Xiang-yi, DING Hua. Hot deformation behaviors and microstructure evolution of a supersaturated nickel-based superalloy [J]. Materials Characterization, 2024, 211: 113915.

[17] YANG Qiu-mei, LIN Yong-cheng, CHEN Ming-song, CHEN Zi-jian. Modeling dynamic recrystallization behavior in a novel HIPed P/M superalloy during high-temperature deformation [J]. Materials, 2022, 15: 4030.

[18] CHEN Jia-yu, DONG Jian-xin, ZHANG Mai-cang, YAO Zhi-hao. Deformation mechanisms in a fine-grained Udimet 720LI nickel-base superalloy with high volume fractions of γ' phases [J]. Materials Science and Engineering A, 2016, 673: 122−134.

[19] LI Zhi-qiang, WANG De-cheng, WANG Li-ping, JIANG Chao, ZHOU Le-yu, ZHOU Zhi-guang, WANG Hui-zhen, Zhang Zi-bo, Zhai Yue-wen. Microstructure evolution characteristics of a powder metallurgy Ni-based superalloy during hot deformation [J]. Materials Today Communications, 2024, 39: 108626.

[20] WEN Hong-ning, TANG Xue-feng, JIN Jun-song, CAI Chao, YANG He-yang, TENG Qing, WEI Qing-song, WANG Xin-yun, ZHENG Chao-wei, HE Ying-jie, GUO Jian-zheng. Effect of extrusion ratios on microstructure evolution and strengthening mechanisms of a novel P/M nickel-based superalloy [J]. Materials Science and Engineering A, 2022, 847: 143356.

[21] ZHU Li-hua, WEI Bing, PAN Hao, XIAO Lei, GUO Jian-zheng, JI Hong-jun. Dynamic deformation mechanism for distinct flow behaviors in FGH4113A superalloy with high γ' content during isothermal compression at sub-/near-/super-solvus temperatures [J]. Materials & Design, 2024, 241: 112890.

[22] SONG Kai, AINDOW M. Grain growth and particle pinning in a model Ni-based superalloy [J]. Materials Science and Engineering A, 2008, 479: 365−372.

[23] ZHAO Jiang, QUAN Guo-zheng, ZHANG Yu-qing, XIONG Wei. Distribution and evolution of low-energy twin boundary density in time-space domain during isothermal compression for Ni80A superalloy [J]. Transactions of Nonferrous Metals Society of China, 2023, 33(11): 3387−3405.

[24] JIANG Wen-xiang, LU Jun-xia, GUAN Hao, WANG Ming-ming, CHENG Xiao-peng, LIU Lin-lin, LIU Xian-qiang, WANG Jin, ZHANG Yue-fei, ZHANG Ze, LIN Wei-tong, HU Jing. Study of pre-precipitated δ phase promoting deformation twinning and recrystallization behavior of Inconel 718 superalloy during hot compression [J]. Materials & Design, 2023, 226: 111693.

[25] XIA Yu-chi, CHEN Xiao-min, LIN Yong-cheng, LU Xian-zheng. Evolution of annealing twins in a hot deformed nickel-based superalloy [J]. Materials, 2022, 15: 7.

[26] QUAN Guo-zheng, ZHANG Yu-qing, ZHANG Pu, MA Yao-yao, WANG Wei-yong. Correspondence between low-energy twin boundary density and thermal-plastic deformation parameters in nickel-based superalloy [J]. Transactions of Nonferrous Metals Society of China, 2021, 31(2): 438−455.

[27] ZHANG Hong-bin, ZHOU Hai-ping, QIN Sheng-xue, LIU Jie, XU Xing-ming. Effect of deformation parameters on twinning evolution during hot deformation in a typical nickel-based superalloy [J]. Materials Science and Engineering A, 2017, 696: 290−298.

[28] LUO Yi-wa, SHI Cheng-bin, XU Hao-chi. Microstructure evolution and hot deformation characteristics of 15Cr−22Ni iron-base superalloy [J]. Journal of Alloys and Compounds, 2023, 938: 168628.

[29] JIANG Yi-ling, LIU Sha-sha, LU Rong-gui, CHENG Xu, LI Jia, CHEN Yang, TIAN Gao-feng. Cellular automata simulation of grain growth of powder metallurgy Ni-based superalloy [J]. Journal of Iron and Steel Research International, 2023, 30(4): 838−848.

[30] YANG Yan-hui, ZHANG Bo-yan, CHEN Xiu-quan, WANG Xiao-xuan, SUN Jing-shi. Modeling and simulation of grain growth for FGH96 superalloy using a developed cellular automaton model [J]. Modelling and Simulation in Materials Science and Engineering, 2024, 32(5): 055011.

[31] YANG Qiu-mei, LIN Yong-cheng, GUO Jian-zheng, WANG Chao, CHEN Zi-jian, CHEN Kai-ge, ZHU Jun-cheng. Spheroidization and dynamic recrystallization mechanisms of a novel HIPed P/M superalloy during hot deformation [J]. Journal of Alloys and Compounds, 2022, 910: 164909.

[32] YANG Jin, LUO Jiao, LI Xiang-yang, LI Miao-quan. Evolution mechanisms of recrystallized grains and twins during isothermal compression and subsequent solution treatment of GH4586 superalloy [J]. Journal of Alloys and Compounds, 2021, 850: 156732.

[33] EBRAHIMI G R, MOMENI A, EZATPOUR H R, JAHAZI M, BOCHER P. Dynamic recrystallization in Monel400 Ni−Cu alloy: Mechanism and role of twinning [J]. Materials Science and Engineering A, 2019, 744: 376−385.

[34] MOMENI A, EBRAHIMI G R, EZATPOUR H R. Modelling the yield point phenomena during deformation at elevated temperatures: Case study on Inconel 600 [J]. Philosophical Magazine, 2018, 98(28): 2543−2561.

[35] GOTTSTEIN G, SHVINDLERMAN L S. Theory of grain boundary motion in the presence of mobile particles [J]. Acta Metallurgica et Materialia, 1993, 41(11): 3267−3275.

[36] LI Zhi-qiang, WANG Jun-sheng, HUANG Hou-bing. Influences of grain/particle interfacial energies on second-phase particle pinning grain coarsening of polycrystalline [J]. Journal of Alloys and Compounds, 2020, 818: 852848.

[37] BABU K A, MANDAL S, KUMAR A, ATHREYA C N, de BOER B, SARMA V S. Characterization of hot deformation behavior of alloy 617 through kinetic analysis, dynamic material modeling and microstructural studies [J]. Materials Science and Engineering A, 2016, 664: 177–187.

[38] BABU K A, MOZUMDER Y H, SAHA R, SARMA V S, Mandal S. Hot-workability of super-304H exhibiting continuous to discontinuous dynamic recrystallization transition [J]. Materials Science and Engineering A, 2018, 734: 269–280.

[39] CHEN Xiao-min, LIN Yong-cheng, CHEN Ming-song, LI Hong-bin, WEN Dong-xu, ZHANG Jin-long, HE Min. Microstructural evolution of a nickel-based superalloy during hot deformation [J]. Materials & Design, 2015, 77: 41−49.

[40] YAN Pei-zhi, WEN Dong-xu, LIU Yang, HUANG Liang, YANG Xiao-li, ZHANG Zhi-cheng, XU Fu-ze, LI Jian-jun. Evolution of microstructure and δ phase in an aging-treated nickel-based superalloy during hot compression [J]. Materials Characterization, 2023, 200: 112876.

[41] ZHANG Jie-ke, CAO Yu, GONG Yu-hao, XIAO Jun, ZHU Yu-long, LUO Rui, HE Qu-bo, LIU Qing. Revealing hot deformation behavior of Inconel X-750 superalloy: A novel hot processing map coupled with grain boundary engineering [J]. Journal of Materials Research and Technology, 2023, 25: 1245−1262.

[42] CHEN Zi-shuai, DONG Rui-feng, LI Jing-nan, DENG Xiang-tao, ZHANG Wei, REN Xiu-lan. Reasons for the stable existence of γ' phase and strengthening mechanism of GH4720Li nickel-based superalloy [J]. Materials Research Express, 2021, 8(5): 56508.

[43] ZHU Zong-xiao, LUO Dong-lei, ZHENG Min, CHEN Wei-hua, WEI Xing-chun, QU Ding-feng, ZHANG Jing-jing, CHEN Jie. Atomic-scale study of the nano-cutting deformation mechanism of nickel-based single crystal superalloy containing Cr, Co, and γ/γ' [J]. Applied Physics A, 2023, 129: 300.

[44] WU Qiong, LI Shu-suo. Alloying element additions to Ni_3Al: Site preferences and effects on elastic properties from first-principles calculations [J]. Computational Materials Science, 2012, 53(1): 436−443.

[45] LEHTINEN A, GRANBERG F, LAURSON L, NORDLUND K, ALAVA M J. Multiscale modeling of dislocation-precipitate interactions in Fe: From molecular dynamics to discrete dislocations [J]. Physical Review E, 2016, 93(1): 013309.

[46] SHI Feng-jian, PIAO Nan-ying, WANG Ji-heng, TAN Hao-tian, GUO Yu-hang, YANG Fei, CHEN Shu-jin, LU Sheng, WANG Ze-xin. Tailoring good combinations between strength and ductility in novel Mg−5Sn−2Al−1Zn alloy via different hot extrusion processes [J]. Transactions of Nonferrous Metals Society of China, 2024, 34(7): 2120−2137.

[47] LIAN Qi-hao, ZHAN Chang-jiang, FENG Hong, YANG Zhen-bo, ZHANG Shu-zhi, HAN Jian-chao, WANG Tao, PENG Fan, CAO Peng. Hot deformation temperature and pre-deformation effect on silicide precipitation behavior of $(TiB+Y_2O_3)$/near α-Ti matrix composite [J]. Transactions of Nonferrous Metals Society of China, 2023, 33(9): 2660−2671.

[48] CHEN Zi-jian, LIN Yong-cheng, HE Dao-guang, LOU Yu-ming, CHEN Ming-song. A unified dislocation density-based model for an aged polycrystalline Ni-based superalloy considering the coupled effects of complicate deformation mechanisms and initial δ phase [J]. Materials Science and Engineering A, 2021, 827: 142062.

热变形 FGH4113A 合金的孪生机制及晶粒尺寸模型

朱峻澄[1,2]，蔺永诚[1,2,3]，陈子健[1,2]，谢永富[4]，杨 晋[4]，Majid NASERI[5]

1. 中南大学 机电工程学院，长沙 410083；
2. 中南大学 极端服役性能精准制造全国重点实验室，长沙 410083；
3. 荣成华东锻压机床股份有限公司，荣成 264300；
4. 贵州安大航空锻造有限责任公司，安顺 561005；
5. South Ural State University, 76 Lenin Av., Chelyabinsk 454080, Russia

摘 要：通过热压缩实验探讨了不同应变速率和变形温度对 FGH4113A 合金显微组织演变的影响。在热压缩变形过程中，动态再结晶和孪生是晶粒组织演变的主要方式，一次 γ'相(γ'_p相)的钉扎作用则是细化晶粒的主要手段。降低应变速率或升高变形温度会促进动态再结晶和孪生的发生，以及 γ'_p相的溶解。当变形温度为 1140 ℃时，γ'_p相的大量溶解及钉扎作用失效导致孪生减弱。发现了一种仅在钉扎作用下出现的孪生机制，即“钉扎孪生”。当位错由于 γ'_p相对晶界的钉扎作用无法通过晶界迁移消耗时，晶粒优先通过孪生来消除位错，以降低局部应变能。建立了考虑钉扎作用的晶粒尺寸预测模型。

关键词：镍基高温合金；热变形；动态再结晶；孪生；γ'相；钉扎作用

(Edited by Bing YANG)